Impacts of Different Cumulus Schemes on the Pathways through which SST Provides Feedback to the Madden–Julian Oscillation

Joshua-Xiouhua Fu

International Pacific Research Center, School of Ocean and Earth Science and Technology, University of Hawai'i at Mānoa, Honolulu, Hawaii, and Institute of Atmospheric Sciences, FuDan University, and Shanghai Institute of Pollution Control and Ecological Security, Shanghai, China

Wanqiu Wang

Climate Prediction Center, NOAA/NWS/NCEP, College Park, Maryland

Yuejian Zhu

Environmental Modeling Center, NOAA/NWS/NCEP, College Park, Maryland

Hong-Li Ren and Xiaolong Jia

National Climate Center, China Meteorological Administration, Beijing, China, and Texas A&M University–Corpus Christi, Corpus Christi, Texas

Toshiaki Shinoda

Texas A&M University–Corpus Christi, Corpus Christi, Texas

(Manuscript received 26 June 2017, in final form 20 February 2018)

ABSTRACT

Six sets of hindcasts conducted with the NCEP GFS have been used to study the SST-feedback processes and assess the relative contributions of atmospheric internal dynamics and SST feedback on the October and November MJO events observed during the DYNAMO IOP (Oct- and Nov-MJO). The hindcasts are carried out with three variants of the Arakawa–Shubert cumulus scheme under TMI and climatological SST conditions. The positive intraseasonal SST anomaly along with its convergent Laplacian produces systematic surface disturbances, which include enhanced surface convergence, evaporation, and equivalent potential temperature no matter which cumulus scheme is used. Whether these surface disturbances can grow into a robust response of MJO convection depends on the characteristics of the cumulus schemes used. If the cumulus scheme is able to amplify the SST-initiated surface disturbances through a strong upward–downward feedback, the model is able to produce a robust MJO convection response to the underlying SST anomaly; otherwise, the model will not produce any significant SST feedback. A new method has been developed to quantify the ''potential'' and ''practical'' contributions of the atmospheric internal dynamics and SST feedback on the MJOs. The present results suggest that, potentially, the SST feedback could have larger contributions than the atmospheric internal dynamics. Practically, the contributions to the Oct- and Nov-MJO events are, respectively, dominated by atmospheric internal dynamics and SST feedback. Averaged over the entire period, the contributions from the atmospheric internal dynamics and SST feedback are about half and half.

Corresponding author: Dr. Joshua-Xiouhua Fu, xfu@hawaii.edu

1. Introduction

Sea surface temperature (SST) distributions in the tropics play important roles in shaping the surface convergence and precipitation of the climatology, seasonal

cycle, and interannual variability (Lindzen and Nigam 1987; Zebiak and Cane 1987; Neelin 1989; Wang and Li 1993; Fu et al. 1994; Fu and Wang 1999; Chiang and Zebiak 2000; Back and Bretherton 2009a,b) as well as intraseasonal variability (Kawamura 1988; Krishnamurti et al. 1988), even for individual convective systems (Li and Carbone 2012; Carbone and Li 2015).

For the tropical climatology, seasonal cycle, and interannual variability (e.g., El Niño–Southern Oscillation), the spatial distributions of SST have long been recognized as the key factor in shaping the patterns of surface convergence and precipitation. However, two different paradigms in literatures have been developed to explain the pathways through which SST influences the surface winds and surface convergence (e.g., Gill 1980; Lindzen and Nigam 1987). Gill (1980) suggested that surface circulations are driven by elevated heating in association with deep convection (the "downward" paradigm), which has been popularly related to the SST in one way or another (e.g., Zebiak and Cane 1987; Neelin and Held 1987; Chiang and Zebiak 2000). On the other hand, Lindzen and Nigam (1987) emphasized that surface winds and convergence are largely driven by the planetary boundary layer (PBL) pressure gradient, which is primarily caused by the SST gradient through vertical mixing (the "upward" paradigm). Neelin (1989) had attempted to reconcile these two paradigms. He acknowledged that these two perspectives are very different in interpreting the key drivers of surface winds and convergence and proved that both approaches actually have similar mathematical expressions and also function very similarly in simple atmospheric models and air–sea coupled models with their own tunable parameters (e.g., Philander et al. 1984; Hirst 1986; Zebiak 1986). In the real world, it is very likely that both the SST gradient and elevated heating contribute to surface winds and convergence (Schneider and Lindzen 1977; Wang and Li 1993; Fu and Wang 1999; Chiang and Zebiak 2000; Wu 2003; Back and Bretherton 2009a,b). On the time scales of individual convective systems, Li and Carbone (2012) and Carbone and Li (2015) have documented that the convergent Laplacian of SST patches[1] (~100 km) can account for 75% of the convective onsets that occurred in the Indo–western Pacific warm pool.

On intraseasonal time scales [e.g., the Madden–Julian oscillation (MJO); Madden and Julian (1971, 1972)], the

associated SST fluctuations have also been deemed to play an important role on the surface winds and precipitation of tropical intraseasonal variability (e.g., Kawamura 1988; Krishnamurti et al. 1988). Three possible impacting processes have been mentioned in the literature: (i) changing convective instability (e.g., Lau and Sui 1997; Stephens et al. 2004; Roxy and Tanimoto 2007); (ii) changing surface evaporation (e.g., Fu et al. 2006, 2008; Marshall et al. 2008; Fu et al. 2015); and (iii) changing surface convergence (e.g., Waliser et al. 1999; Maloney and Kiehl 2002; Fu et al. 2008; Hsu and Li 2012; Fu et al. 2015).

The estimate with observations suggests that the increase of evaporation directly from a positive intraseasonal SST anomaly is about $10\,\mathrm{W\,m^{-2}}$, which accounts for less than 10% of the intraseasonal precipitation variability (e.g., Shinoda et al. 1998; Riley Dellaripa and Maloney 2015; de Szoeke et al. 2015). The surface convergence directly driven by the SST gradient accounts for about 10%–25% of the total convergence in association with the MJO convection (e.g., Maloney and Kiehl 2002; Hendon 2005; Hsu and Li 2012). Using a hybrid coupled model developed at the University of Hawai'i at Mānoa, Fu et al. (2003) and Fu and Wang (2004) found that active air–sea coupling enhances the intraseasonal intensity by about 50% measured with wavenumber–frequency spectra. Fu et al. (2007, 2008, 2013, 2015) showed that active air–sea coupling extends the potential predictability and forecasting skill of intraseasonal variability by at least one week. Because of the relatively small direct contribution of SST to the intraseasonal precipitation anomaly estimated from the observations, various biases existing in coupled models (e.g., Inness et al. 2003; Fu et al. 2003; DeMott et al. 2015), and negligible or negative impacts of air–sea coupling on MJO simulations in some coupled models (e.g., Hendon 2000; Grabowski 2006; Newman et al. 2009; Ajayamohan et al. 2011), how and to what degree the intraseasonal SST anomaly impacts the atmospheric intraseasonal variability remains elusive (Miura et al. 2007; National Research Council 2010). New approaches are needed to better understand the SST-feedback processes and new methods should be developed to better quantify the contribution of SST feedback on the MJO.

In a series of previous studies (e.g., Fu et al. 2008, 2013, 2015; Pegion and Kirtman 2008; de Boisseson et al. 2012; Wang et al. 2015), it is proven that the initialized atmosphere-only hindcast is a suitable way to study SST feedback on MJO simulations, which effectively overcomes the mean-state bias problems plaguing the coupled models. Along this line, a series of hindcast experiments with different cumulus schemes under different SST conditions have been carried out with the NCEP Global Forecast System (GFS) to study the

---

[1] The convergent Laplacian of SST represents the convergence directly induced by the SST gradient through vertical mixing, which is calculated as $(-\nabla^2 \mathrm{SST})$ with a positive (negative) value representing convergence (divergence) in this study.

impacts of SST feedback on MJO simulations (Wang et al. 2015; Fu et al. 2017). It is found that the importance of SST feedback largely varies among different cumulus schemes and SST conditions used. The MJO that occurred in October 2011 during the DYNAMO period (hereafter referred to as Oct-MJO) is largely driven by atmospheric internal dynamics whereas the MJO generated in early November during DYNAMO (hereafter referred to as Nov-MJO) is strongly coupled to the underlying ocean. In the present study, the diverse SST-feedback processes in association with these two MJO events under different cumulus schemes are investigated. New methods are developed to distinguish the relative contributions of atmospheric internal dynamics and air–sea coupling on the MJOs.

The remaining article is structured as follows. In section 2, the model is described and sensitivity experiments are briefed. Section 3 documents the gross SST-feedback processes under different cumulus schemes. Section 4 focuses on the specific feedback processes essential to the Nov-MJO. Section 5 develops new methods to quantify the relative contributions of atmospheric internal dynamics and SST feedback on the MJOs. Finally, discussion and conclusions are given in section 6.

2. Model and sensitivity experiments

The NCEP GFS (version 11.0) used to generate hindcasts for this study has a horizontal resolution of T126 with 64 vertical levels. The atmospheric model physics are the same as that of the CFSv2 (Saha et al. 2014). In addition to the simplified Arakawa–Schubert (SAS) scheme used for the CFSv2, the GFS has two other built-in alternative convection schemes: the relaxed Arakawa–Schubert (RAS) and simplified Arakawa–Schubert, version 2 (SAS2). A brief summary of these three convection schemes is given here. More details can be found in Wang et al. (2015) and references therein.

The SAS is the scheme used in the CFSv2, which is based on Arakawa and Schubert (1974) and modified by Pan and Wu (1995). The RAS is developed by Moorthi and Suarez (1992, 1999), which simplified the treatments of normalized mass flux and relaxed the requirement of "quasi-equilibrium" in the original Arakawa–Schubert (AS) scheme. The SAS2 (Han and Pan 2011) is the scheme used in the current operational GFS, which includes modifications to increase cloud-base mass flux and enhance the sensitivity of entrainment and detrainment to environmental moisture (Bechtold et al. 2008).

In total, six sets of initialized hindcasts carried out with the GFS during the intensive operational period

(IOP) of DYNAMO (1 October 2011–15 January 2012) are used, respectively, with three cumulus schemes under two SST settings: TMI daily analysis (Wentz et al. 2000) and the long-term climatology (hereafter referred as TMI and CLIM). The same initial conditions from the NCEP Climate Forecast System Reanalysis (CFSR; Saha et al. 2010) were used for the six sets of hindcasts. The TMI includes realistic intraseasonal SST anomalies while the CLIM contains no intraseasonal SST variability. In this study, the differences between the TMI runs and CLIM runs are used to represent the effects of SST feedback.

Wang et al. (2015) and Fu et al. (2017) have validated the hindcasts with observations. It is found that the runs with the RAS scheme forced by TMI SST largely reproduce the observed Oct- and Nov-MJO events during DYNAMO in terms of intensity, temporal evolutions, and phase relationships between convection and specified intraseasonal SST anomalies. On the other hand, the results with SAS2 are consistently weaker than that with the RAS even though the same initial and SST conditions are used. The results with the SAS fall in the middle. Therefore, it is reasonable to assume that the SST-feedback processes in the runs with the RAS scheme forced by TMI SST reflect what happened in nature. The differences among the runs with RAS, SAS, and SAS2 schemes will reveal different SST-feedback processes. Since diverse cumulus schemes have been used in present-day global models, examining the responses of three cumulus parameterizations to the same SST forcing will shed light on the possible causes of the diverse SST-feedback processes in community models (e.g., CMIP6 models; Eyring et al. 2016).

3. SST-feedback processes under different cumulus parameterizations

To reveal the diverse SST-feedback processes under three different cumulus parameterizations, Figs. 1, 2, and 3 present the responses of OLR, surface convergence, and latent heat flux anomalies to the same TMI SST anomaly within the first 10-day hindcasts for the first two MJO events that occurred during the DYNAMO period. As noticed in our previous study (Fu et al. 2017), both the RAS and SAS2 show much faster responses than the SAS during first 4 days for the convection (Figs. 1a–f), but surface convergence (Figs. 2a–f) and latent heat flux (Figs. 3a–f) are very similar under all three schemes. Since the same initial conditions have been used for the TMI and CLIM runs, the differences of surface convergence and latent heat flux between these two runs in the first few days are basically driven by an intraseasonally varying SST anomaly. The deep convection in the RAS and SAS2
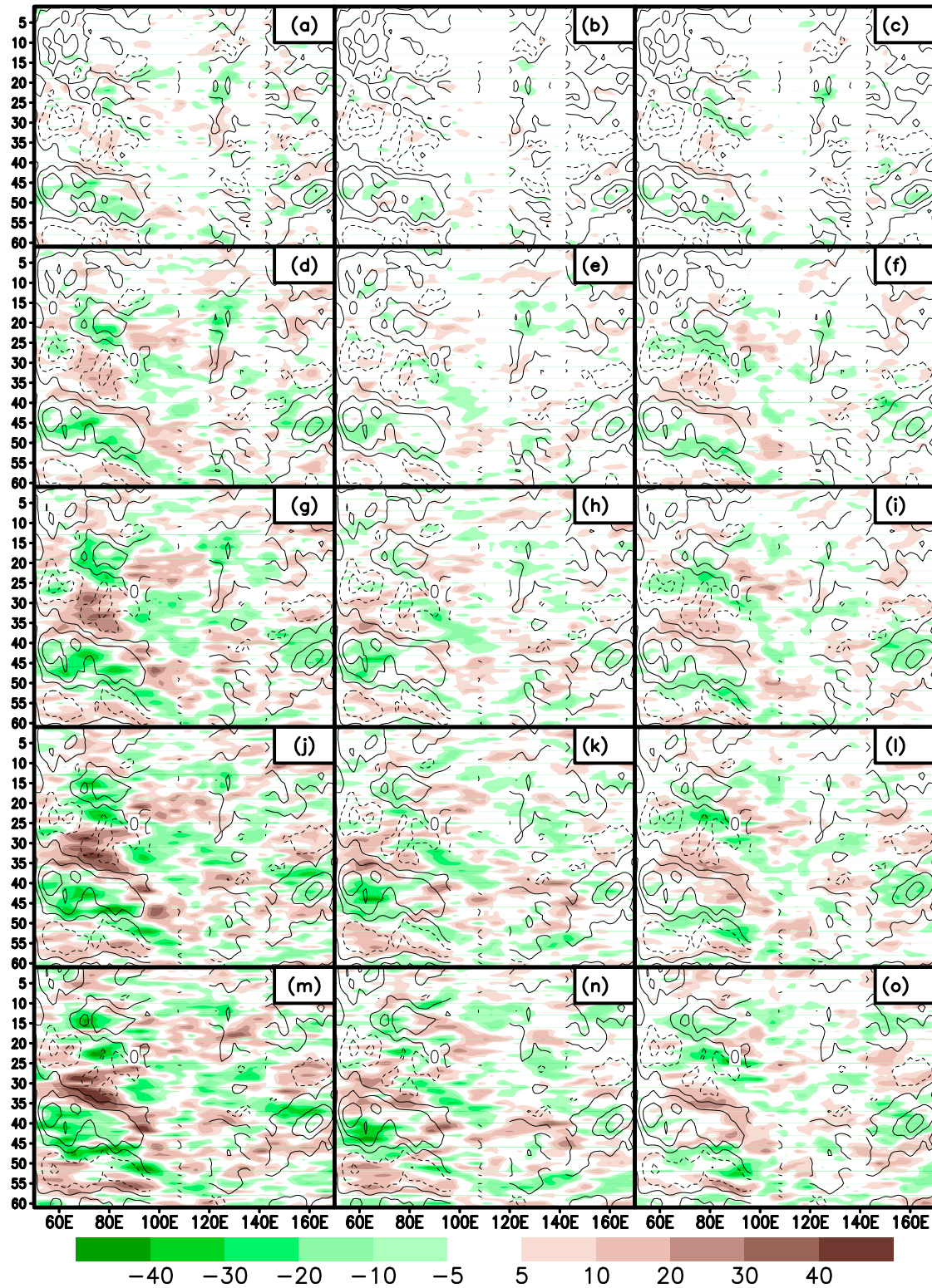
FIG. 1. Longitude–time evolutions of simulated OLR (colored shading, W m^{-2}) and SST anomalies [contours; contour interval (CI): 0.2°C] averaged between 10°S and 10°N with the (left) RAS, (middle) SAS, and (right) SAS2 cumulus schemes at lead times of days (from top to bottom) 2, 4, 6, 8, and 10 forced with TMI SST. Therefore, the corresponding first day of the ordinate in each row is 2, 4, 6, 8, and 10 Oct 2011, from top to bottom, respectively.
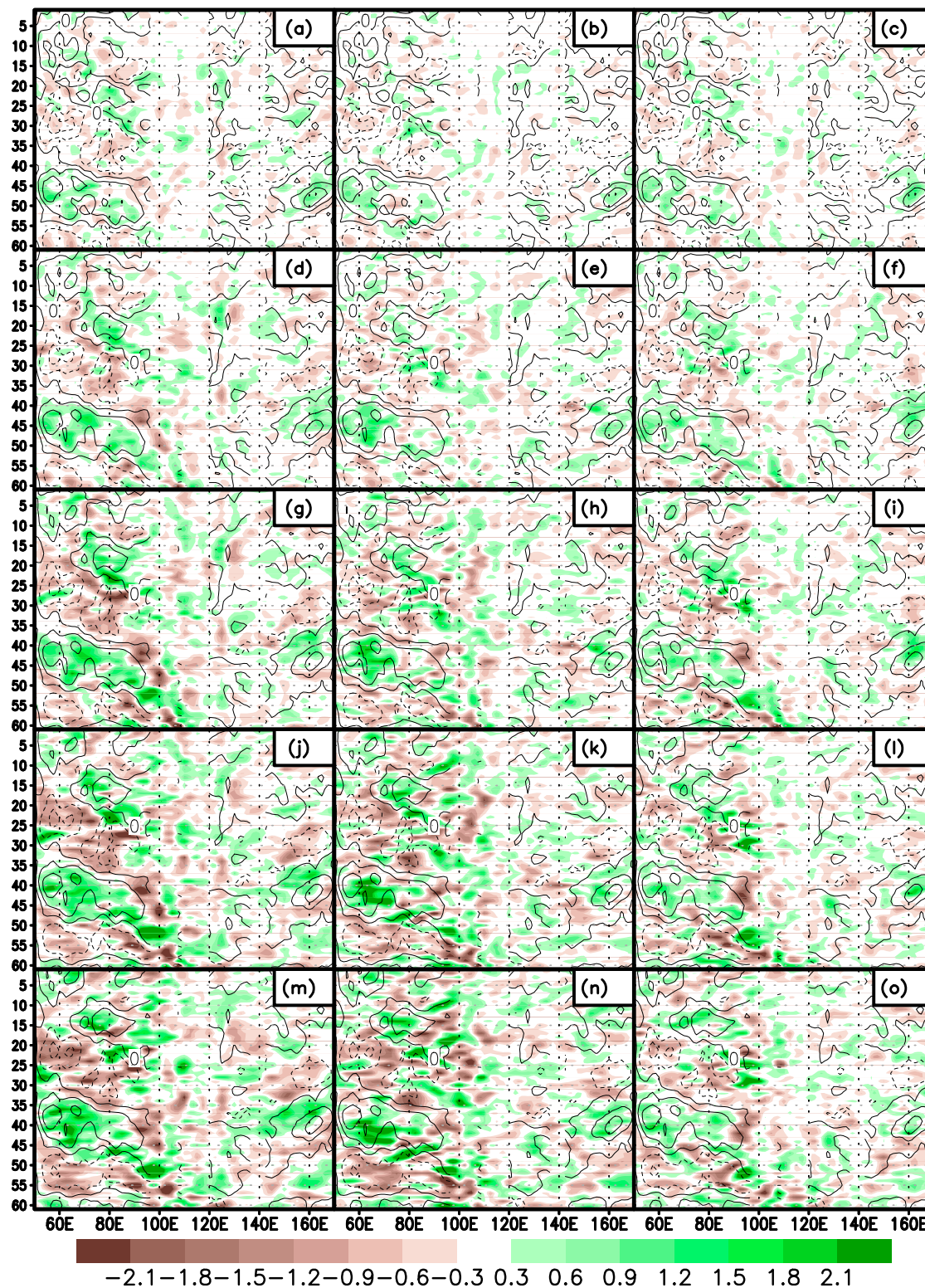
FIG. 2. As in Fig. 1, but for longitude–time evolutions of simulated surface convergence (colored shading, $1 \times 10^{-6}\,\mathrm{s}^{-1}$) and SST anomalies (contours, CI: 0.2°C) averaged between 10°S and 10°N.
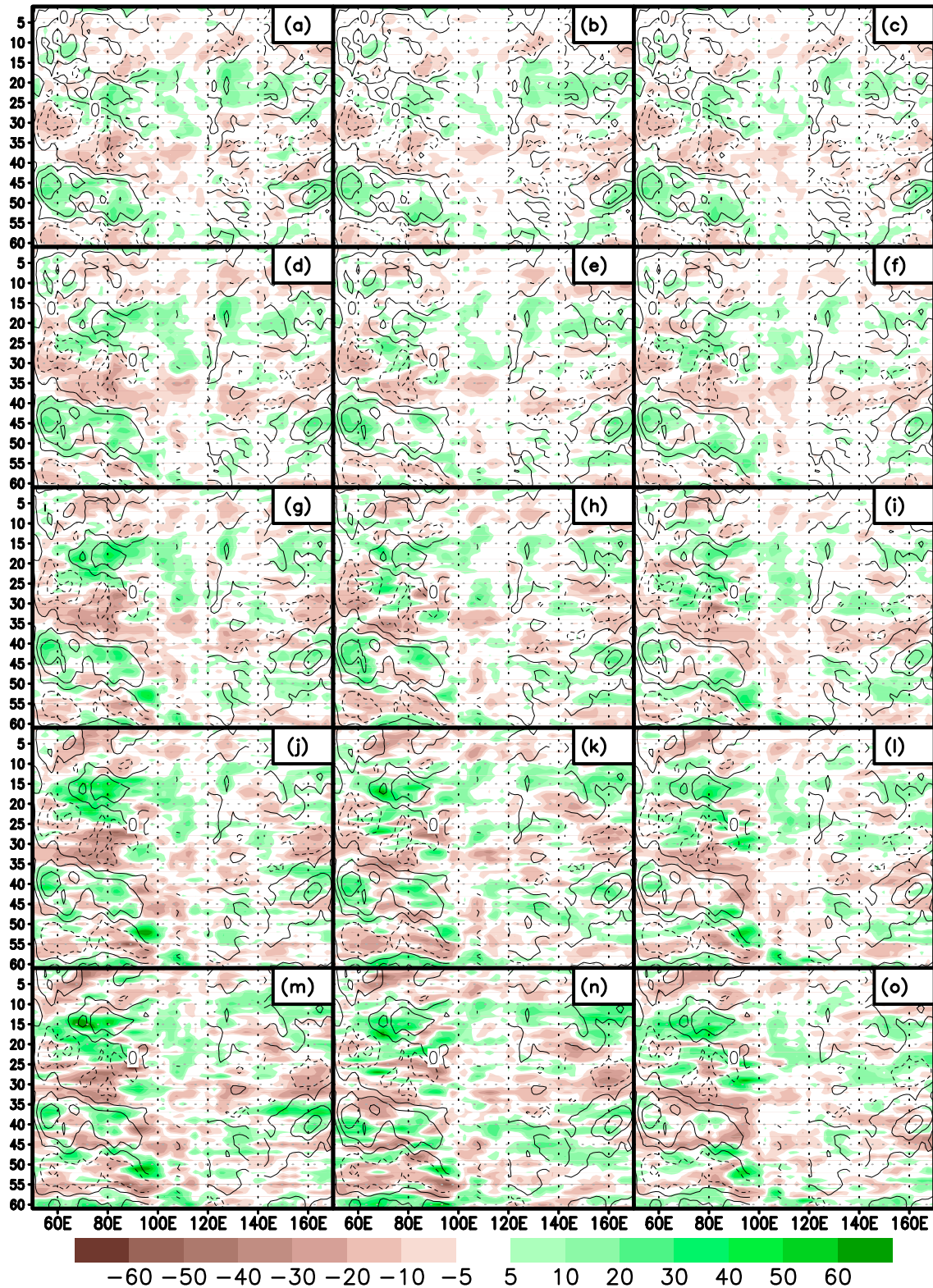
FIG. 3. As in Fig. 2, but for surface latent heat flux (colored shading, W m^{-2}) and SST anomalies (contours, CI: 0.2°C).

schemes is more sensitive to these surface disturbances than that in the SAS scheme.

When the lead time increases from day 4 to day 10, the OLR responses to the SST anomaly in the SAS2 scheme remain almost unchanged (Figs. 1f,i,l,o), but grow rapidly in the RAS and SAS schemes (Figs. 1d,g,j,m and 1e, h,k,n). In association with the significantly enhanced convection, the surface convergence in the RAS and SAS (Figs. 2d,g,j,m and 2e,h,k,n) also shows much more robust growth than that in the SAS2 (Figs. 2f,i,l,o). The perturbations of surface latent heat flux anomalies, however, are very similar among the three cumulus schemes at all lead times (Figs. 3d,g,j,m and 3e,h,k,n and 3f,i,l,o). This result suggests that the coupling between deep convection and surface convergence is more important (Kim and Seo 2018) than the coupling with surface latent heat flux in capturing the SST feedback.

It is well known that tropical surface winds and convergence are controlled by SST-gradient-forced upward impacts (e.g., Lindzen and Nigam 1987) and atmospheric-heating-driven downward impacts (e.g., Gill 1980). In the experiments with three different cumulus parameterizations, the direct contributions from SST-gradient forcing should be almost the same because the underlying SST anomaly is the same. The differences shown in Figs. 1, 2, and 3, thus, are largely due to the diverse responses of different cumulus parameterizations to the underlying SST anomaly. To assess the relative impacts of surface forcing and elevated heating on near-surface disturbances, we further examine the relationships[2] among the anomalies of SST, convergent Laplacian of SST (LSST; Li and Carbone 2012; Carbone and Li 2015), convection, surface convergence, and latent heat flux under three different cumulus schemes at different lead times (Fig. 4). The SST and LSST show significant correlations with convection only within the first few days.

The LSST is highly correlated with the SST under all lead times (Fig. 4), which indicates that the positive SST anomaly is largely collocated with SST-gradient-induced convergence. The latter usually have smaller spatial scales than the former (Li and Carbone 2012). As expected from Figs. 1 and 2, the convection has much stronger correlation (or coupling) with surface convergence in the RAS and SAS than that in the SAS2. The convection, SST, and LSST have very similar correlations with surface convergence within the first 5 days for
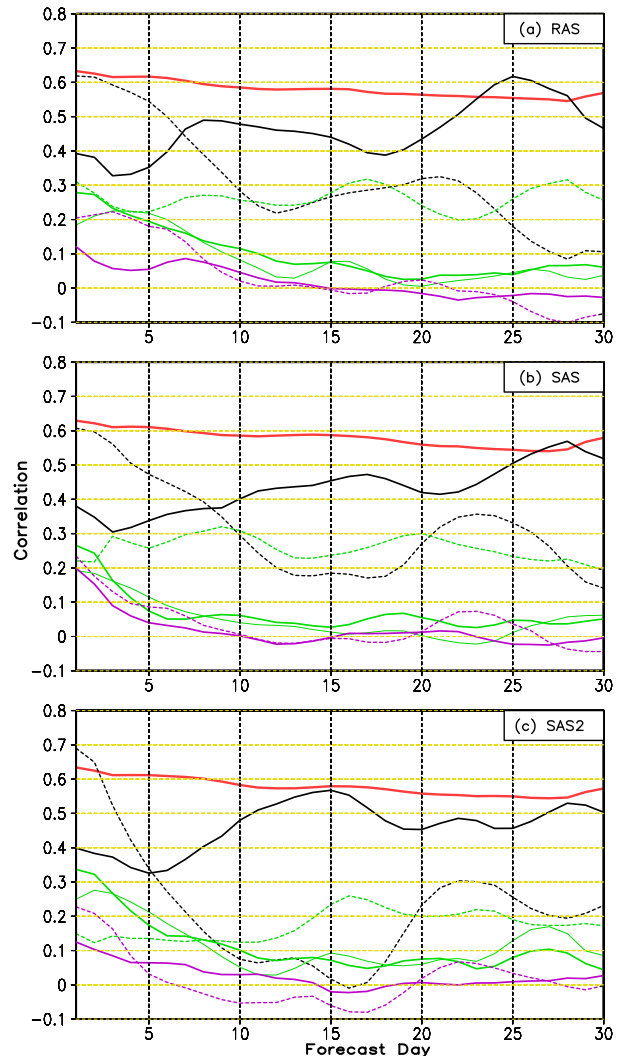

FIG. 4. The correlation coefficients between two longitude–time fields (as in Figs. 1–3) as function of lead time (days) with the (a) RAS, (b) SAS, and (c) SAS2 schemes. The red line is between the convergent SST Laplacian (−lsst) and SST, the black solid (dashed) lines are between the −OLR (SST) and surface latent heat flux, the green solid thick (thin) lines are between −lsst (SST) and surface convergence, the green dashed line is between −OLR and surface convergence, and the purple solid (dashed) lines are between −lsst (SST) and −OLR.

the RAS and SAS (Figs. 4a,b), and slightly longer than a week for the SAS2 (Fig. 4c). Afterward, the convection has much higher correlation with surface convergence than the SST and LSST,[3] which means that the coupling between the elevated heating and overturning circulation becomes the major controlling factor of the surface

---

[2] The relationships are illustrated with the pattern correlation coefficients between two longitude–time fields at different lead times (e.g., the SST and OLR correlations at lead time of day 10 are calculated from Figs. 1m,n,o, respectively, for the RAS, SAS, and SAS2 schemes).

[3] This is also the case even after considering the phase lag between SST/LSST and surface convergence (figures not shown).

disturbances (e.g., Gill 1980). For the SAS2 scheme (Fig. 4c), the delayed and weak coupling between convection and surface convergence is likely responsible for the weak SST feedback shown in Fig. 1.

The surface latent heat flux is highly correlated with both the underlying SST anomaly and convection (Fig. 4). Before and after the first week, the SST and convection, respectively, have higher correlations with the surface latent heat flux. The correlations between the SST and surface latent heat flux drop much faster in the SAS2 scheme than that in the RAS and SAS schemes. As surface latent heat flux is largely induced by surface winds associated with the convection (Riley Dellaripa and Maloney 2015), the persistent correlations in the RAS and SAS schemes may not mean that the SST has larger impacts on surface latent heat flux in these two schemes, rather because a near-quadrature phase relationship between the convection and SST can be maintained in the RAS and SAS schemes, but not in the SAS2 scheme (Wang et al. 2015; Fu et al. 2017).

To illustrate the different atmospheric responses to the same SST anomaly in the RAS and SAS2 schemes, the perturbation growths among the surface convergence, latent heat flux, and convection as well as the relationship between the convergence and LSST have been shown in Fig. 5 as scatterplots at different lead times. On day 3, all perturbations have similar magnitudes no matter whether the RAS or the SAS2 scheme is used (Figs. 5a,b). As lead time increases, the perturbations of latent heat flux are very similar between the RAS and SAS2 schemes (Figs. 5d,g,j,m). The perturbations of convergence, however, are much larger in the RAS scheme than that in the SAS2 scheme (Figs. 5e,h,k,n). The LSST shows some significant correlation with surface convergence only within the first 10 days (Figs. 5c,f, i,l,o). This result suggests that initially the runs with either the RAS or SAS2 scheme have very similar responses to the underlying SST anomaly. The initial perturbations can only be significantly amplified with the RAS scheme because of the strong coupling between convection and surface convergence, which plays a key role in sustaining a robust MJO in models (Kim and Seo 2018), but not with the SAS2 scheme.

To further understand the impacts of SST and convection on near-surface thermodynamics, we calculated the correlations of SST and convection with three surface thermodynamic variables: air temperature, specific humidity, and equivalent potential temperature (Fig. 6) under three cumulus schemes at different lead times. It is found that the SST has larger impacts on specific humidity and equivalent potential temperature within the first two weeks. Afterward, the convection plays a larger

role. For surface air temperature, the SST always has a stronger impact than the convection.

4. SST-feedback processes associated with the Nov-MJO during DYNAMO

In our previous studies (Fu et al. 2015, 2017; Wang et al. 2015), we have shown that the Nov-MJO during the DYNAMO period is strongly coupled to the underlying ocean. While forced by the same TMI SST, the atmospheric responses with the RAS scheme are much stronger than that with the SAS2 scheme. In this section, detailed analysis has been carried out to understand the different SST-feedback processes in association with the RAS and SAS2 schemes for the Nov-MJO.

Figures 7 and 8 show the spatial patterns of the SST anomaly and the responses of OLR and some surface variables with the RAS and SAS2 schemes, respectively, at day 5 and day 10. At day 5 (Fig. 7), a patch of coherent positive SST anomaly has formed over the equatorial western Indian Ocean along with suppressed convection. As shown in Fig. 4, the convergent Laplacian of SST well collocates with the positive SST anomaly (Figs. 7a,b), which forces surface convergence over the positive SST anomaly no matter which cumulus scheme is used (Figs. 7c,d). At the same time, positive surface heat flux (Figs. 7e,f) and equivalent potential temperature (Figs. 7g,h) perturbations also tend to appear over the positive SST anomaly. At this stage, the surface disturbances are largely forced by the intraseasonally varying SST anomaly since no organized convection has emerged over the tropical Indian Ocean yet.

At day 10 (Fig. 8), the positive SST anomaly has expanded to the entire equatorial Indian Ocean, as does the convergent Laplacian of SST (Figs. 8a,b). The organized convection occurs in the case with the RAS scheme (Figs. 8a,c,e,g), but not with the SAS2 scheme (Figs. 8b,d,f,h) although the associated patterns of latent heat flux (Figs. 8e,f) and equivalent potential temperature (Figs. 8g,h), and to some degree, surface convergence (Figs. 8c,d) anomalies, are very similar between the two schemes. This result indicates that the positive SST anomaly and its convergent Laplacian are able to produce coherent surface convergence, significant latent heat flux, and equivalent potential temperature disturbances (e.g., Figs. 7 and 8). Whether these surface disturbances can develop into robust convection responses largely depends on the characteristics of cumulus schemes used. Possible misrepresentation of convective processes in the SAS2 scheme will be discussed in the last section.

In addition to the spatial patterns at day 5 and day 10, Fig. 9 shows the 30-day temporal evolutions of Nov-MJO-related convection and surface disturbances averaged over
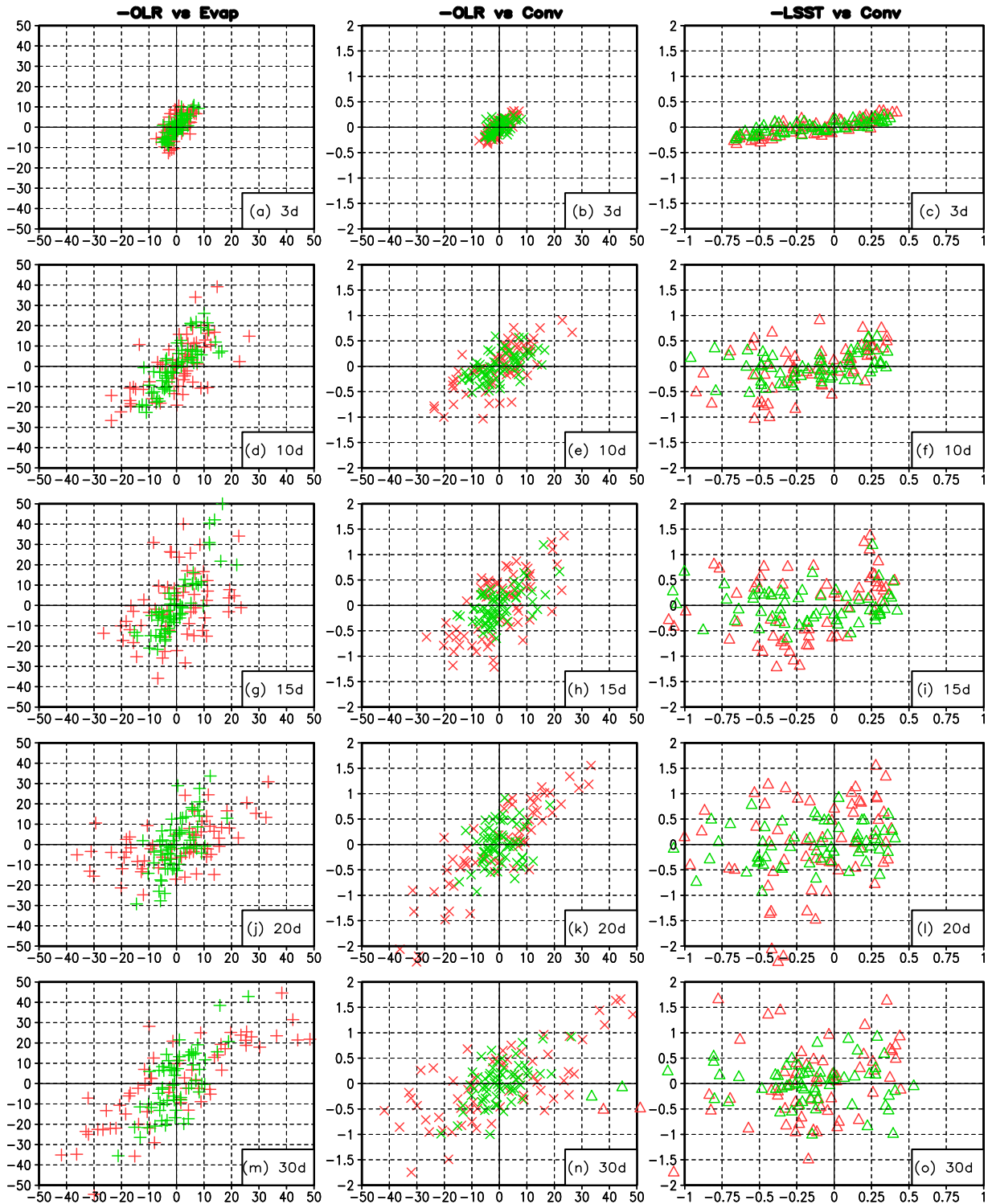
FIG. 5. The scatterplots of the convection ($-$OLR, W m^{-2}, abscissa) vs (left) surface latent heat flux (Evap, W m^{-2}, ordinate) and (center) surface convergence (Conv, 10^{-6} s^{-1}, ordinate) and (right) convergent Laplacian of SST ($-$LSST, 10^{-12} °C m^{-2}, abscissa) vs surface convergence (Conv, 10^{-6} s^{-1}, ordinate) at lead times of days 3, 10, 15, 20, and 30 for the RAS (red) and SAS2 (green) schemes.
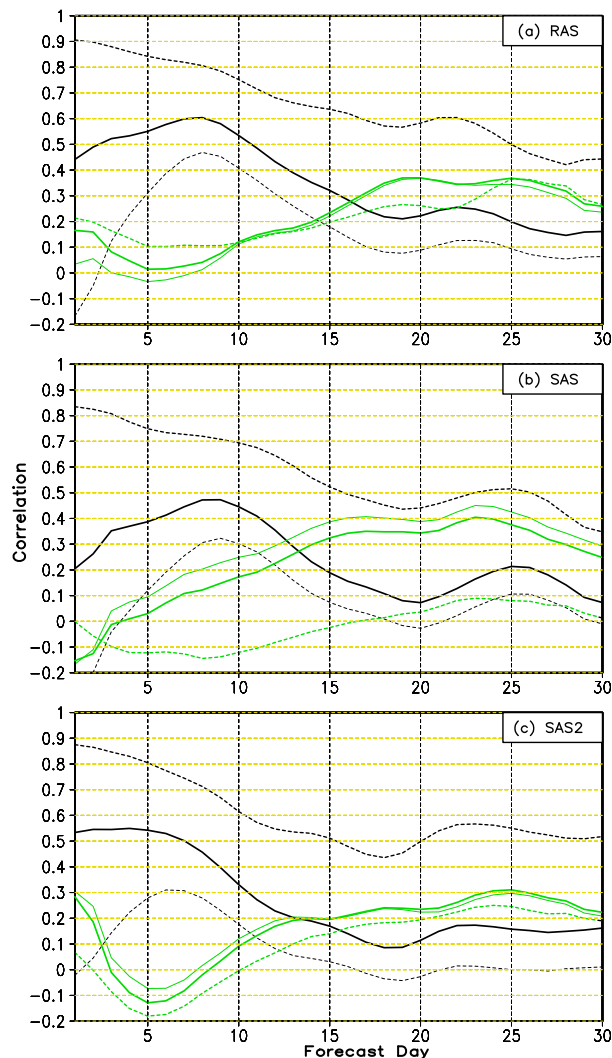
FIG. 6. The correlation coefficients between two longitude–time fields (as in Figs. 1–3) as function of lead time (days) with the (a) RAS, (b) SAS, and (c) SAS2 schemes. The black solid line is between the SST and surface equivalent potential temperature, the black thick (thin) dashed lines are between the SST and surface air temperature (specific humidity), the green dashed line is between convection and equivalent potential temperature, and the green solid thick (thin) lines are between convection and surface air temperature (specific humidity).

the equatorial western Indian Ocean (10°S–10°N, 60°–80°E) under the RAS and SAS2 schemes. Forced with the same positive SST anomaly and its convergent Laplacian, the convection response in the SAS2 scheme is systematically weaker[4] than that in the RAS scheme (Fig. 9a).

During the course of the 30-day integration, the perturbations of the surface convergence and equivalent potential temperature, and to some degree the surface evaporation in the RAS scheme, are consistently larger than that in the SAS2 scheme, further corroborating that much stronger coupling between convection and near-surface disturbances can be sustained in the RAS, but not the SAS2 scheme.

The above analysis further confirms that the initial surface disturbances in response to the underlying SST anomaly are very similar no matter which cumulus scheme is used (Figs. 7, 8). The resultant Nov-MJO differences between the runs with the RAS and SAS2 schemes can be attributed to different upward impact processes of surface disturbances (or the capability to develop a robust convection response) and associated downward feedback processes from the elevated heating. To gain further insights on the different upward–downward feedback[5] processes with the RAS and SAS2 schemes, Figs. 10 and 11 compare their vertical structures during the Nov-MJO passage over the tropical Indian Ocean.

As shown before at day 5 (Fig. 7), the positive SST anomaly in the western equatorial Indian Ocean and its convergent Laplacian start to initiate some surface disturbances: for example, the positive evaporation just west of 60°E and surface convergence over the convergent Laplacian (Figs. 7c,d and 11a,b). However, no large-scale organized convection develops yet (Figs. 10a,b and 11a,b). On day 10 (Figs. 10c,d and 11c,d), surface convergence and evaporation rapidly moisten the PBL and increase surface equivalent potential temperature. These surface disturbances excite vigorous organized convection and significant upward moisture transport in the RAS scheme (Fig. 10c), leading to the formation of shallow heating in the east and uplifted heating along with stratiform rainfall in the west (Fig. 11c). The coexistence of robust positive temperature (Fig. 10c) and heating (Fig. 11c) anomalies in the upper troposphere indicates the generation of eddy available potential energy by the convection (e.g., Lau and Lau 1992; Hendon and Salby 1994; Fu and Wang 2009), which in

---

[4] The case with the SAS2 scheme has later onset, a shorter convection period, and much weaker amplitude than the case with the RAS scheme (Fig. 9a).

[5] The ''upward–downward feedback'' referred here comprises a chain of processes: the positive SST anomaly and associated convergent Laplacian enhance surface convergence, evaporation, and convective instability; these surface disturbances trigger the development of deep convection through an upward impact (Lindzen and Nigam 1987); the elevated diabatic heating in association with the deep convection, on the other hand, enhances surface disturbances through a downward impact (Gill 1980). The resultant mutual intensifications of surface disturbances and elevated heating are called upward–downward feedback in this study.
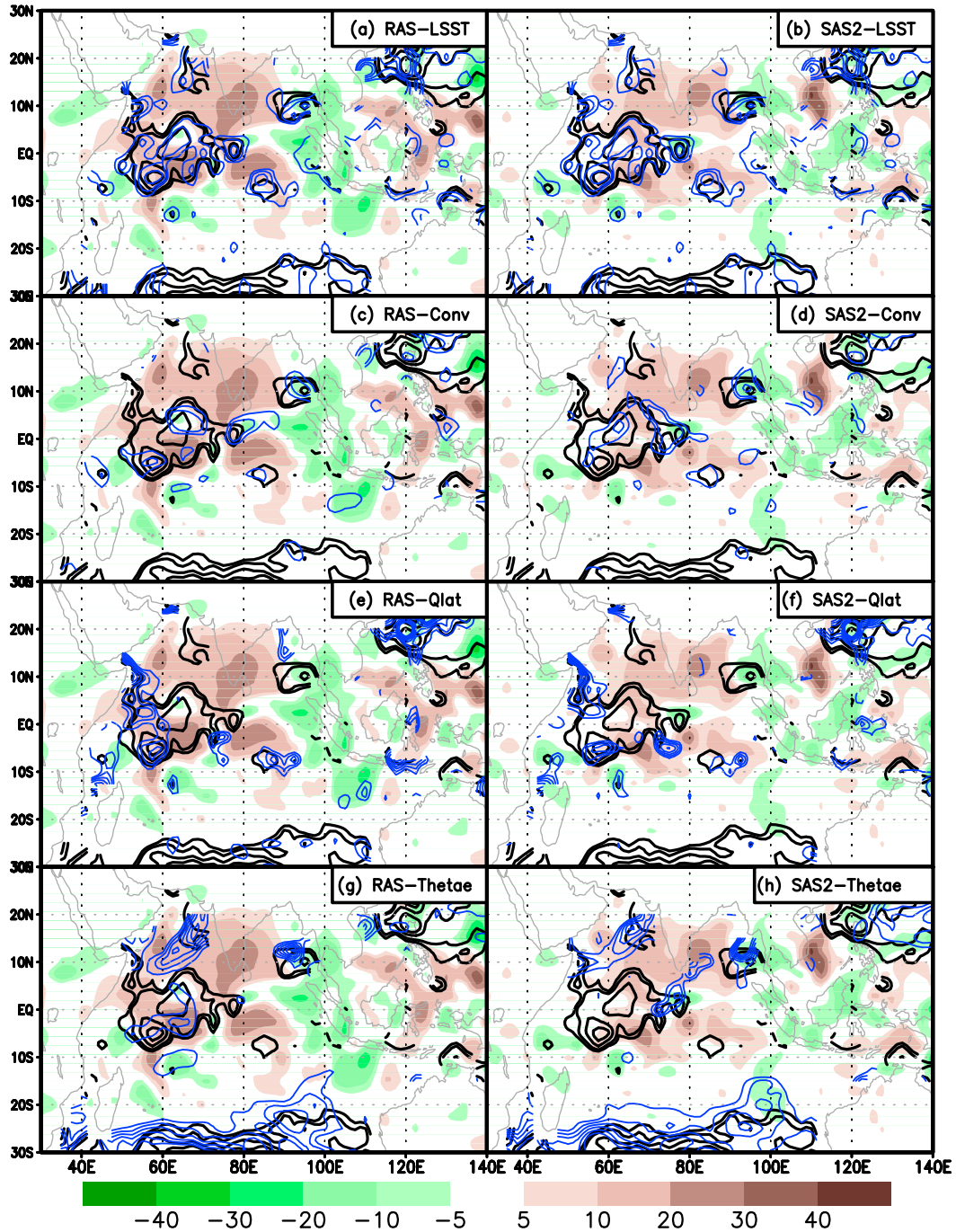
FIG. 7. Spatial distributions of SST (solid black contours: 0.1°, 0.2°, 0.4°, and 0.6°C) and convection (colored shading, OLR, W m^{-2}) anomalies along with the perturbations of the (a),(b) convergent Laplacian of SST (blue contours: 1, 3, 6, 9×10^{-12} °C m^{-2}); (c),(d) surface convergence (blue contours: 1, 2, 4, 6×10^{-6} s^{-1}); (e),(f) surface latent heat flux (blue contours: 5, 10, 15, 20, 25, 30, 35 W m^{-2}); and (g),(h) equivalent potential temperature (blue contours: 0.3, 0.6, 0.9, 1.2, 1.5, and 1.8 K), respectively, for the RAS and SAS2 schemes at the fifth day after initialization on 7 Nov 2011.

turn sustains a robust large-scale overturning circulation (Fu et al. 2015). For the SAS2 scheme, only scattered convection develops along with very weak tropospheric moistening (Fig. 10d) and heating (Fig. 11d). The lack of

tropospheric moistening hinders the formation of stratiform rainfall (Fu and Wang 2009), thus there is no robust upper-tropospheric heating and warming, no apparent generation of eddy available potential energy,
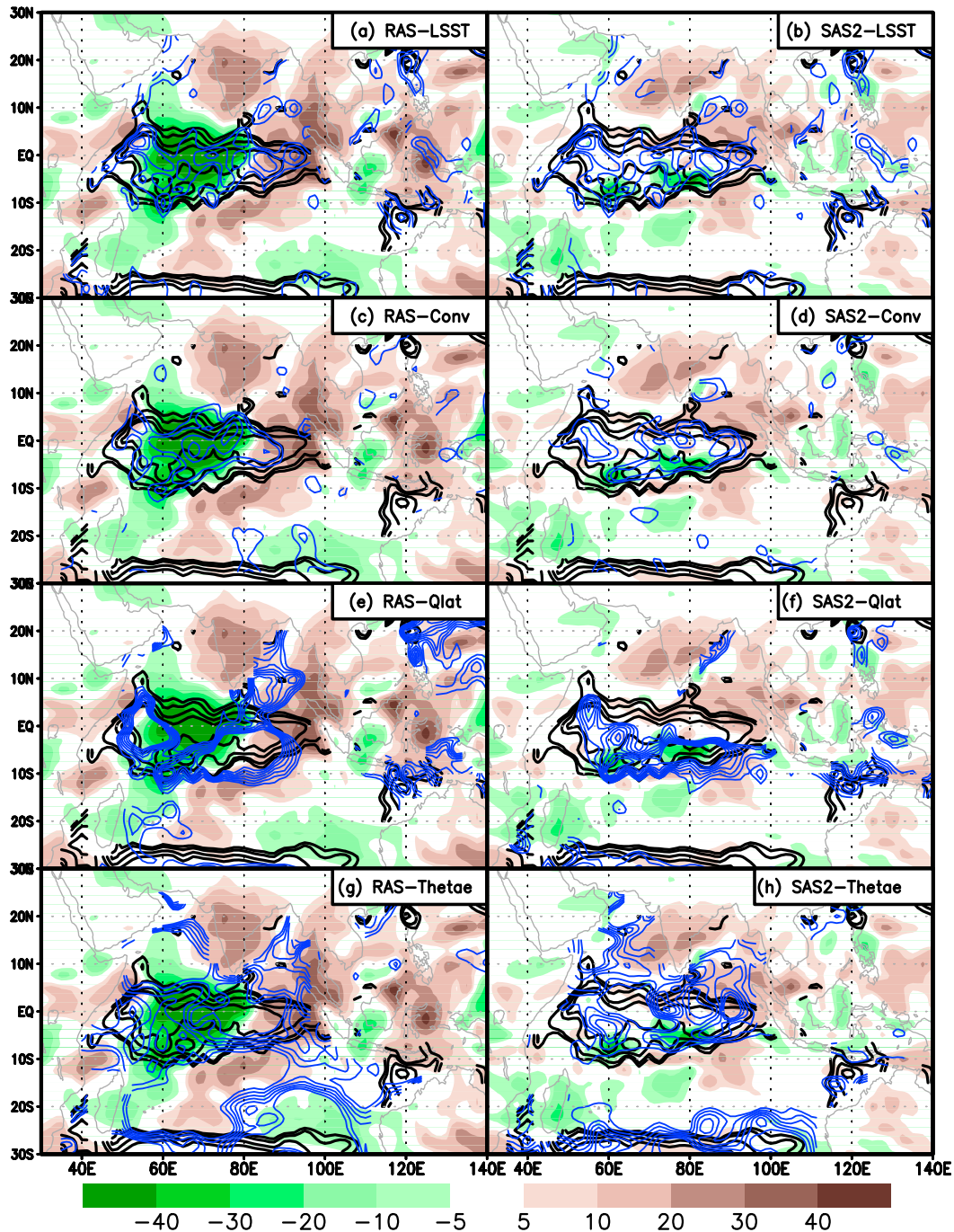
FIG. 8. As in Fig. 7, but for the RAS and SAS2 schemes at the 10th day after initialization on 7 Nov 2011.

and no sustained overturning circulation (Wang et al. 2017).

It seems that the formations of a robust overturning circulation (Fig. 10c), a tropospheric heating dipole, and a low sea level pressure (SLP) tongue (Fig. 11c) are essential ingredients to amplify the surface disturbances initiated by the intraseasonally varying SST anomaly. The intensified

circulation further enhances surface evaporation. The low SLP tongue intensifies surface convergence ahead of and below the deep convection. Both of them help increase surface equivalent potential temperature, and thus column convective instability. All these processes further intensify the convection and tropospheric moistening. The tropospheric downward motion (Fig. 10c) and cooling (Fig. 11c)
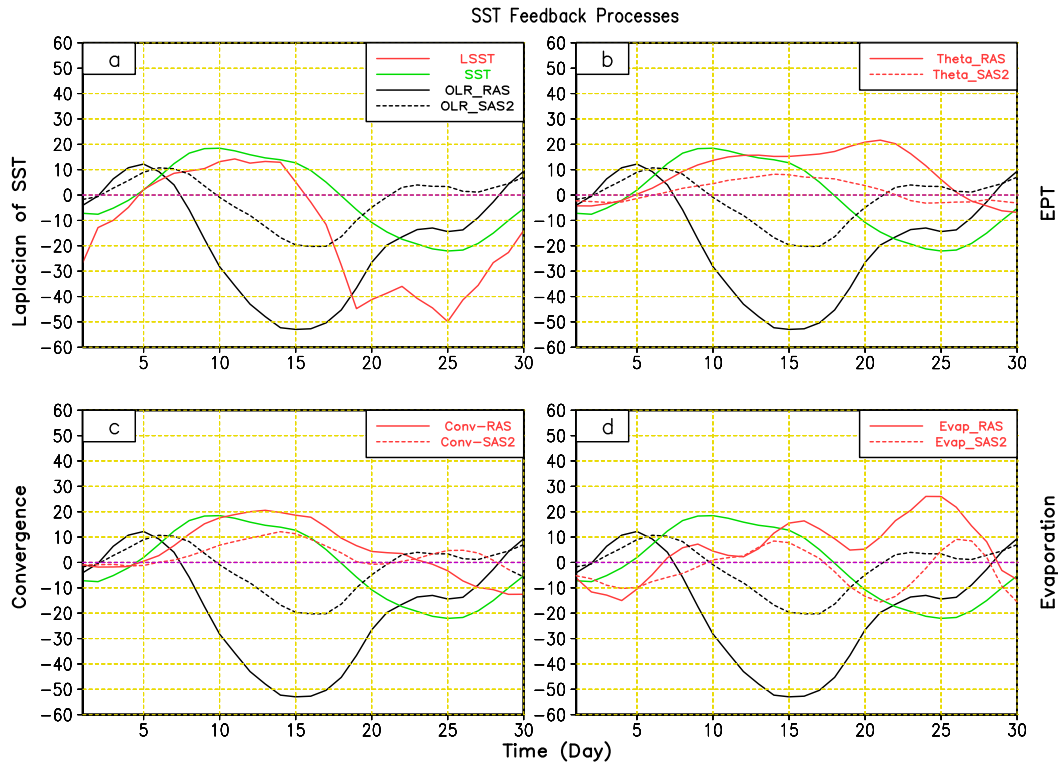
SST Feedback Processes

FIG. 9. Box-averaged (10°S–10°N, 60°–80°E) temporal evolutions of SST (green line, °C/50) and OLR anomalies (W m^{-2}, black dashed line: SAS2, black solid line: RAS), plus (a) convergent Laplacian of SST (red line, 10^{-12} °C m^{-2}/20), (b) equivalent potential temperature (K/10, red dashed line: SAS2, red solid line: RAS), (c) surface convergence (10^{-6} s^{-1}/10, red dashed line: SAS2, red solid line: RAS), and (d) surface evaporation (W m^{-2}, red dashed line: SAS2, red solid line: RAS) anomalies.

ahead of the convection will delay the onset of deep convection and favor the accumulation of moisture supplied from surface convergence and evaporation within the PBL, thus leading to a backward-tilting moisture structure (Figs. 10c,e,g).

When the lead time increases to day 15 and day 20, the upward–downward feedbacks between SST-initiated surface disturbances and deep convection intensify significantly in the RAS scheme (Figs. 10e,g and 11e,g), but remain very weak in the SAS2 scheme (Figs. 10f,h and 11f,h). The strong upward–downward feedback in the RAS scheme significantly moistens the troposphere, warms the upper troposphere, and moves the MJO eastward (Figs. 10e,g and 11e,g). In the SAS2 scheme, the upward–downward feedback is very weak, thus the associated tropospheric moistening and convection resulting from SST-initiated surface disturbances are systematically weaker than that in the RAS scheme (Figs. 10f,h and 11f,h).

The above results suggest that no matter which cumulus parameterization scheme is used, a positive intraseasonal SST anomaly will induce systematic surface disturbances (e.g., surface convergence from the convergent Laplacian of SST, enhanced surface evaporation, and equivalent

potential temperature). Whether a model can produce robust SST feedback to the atmosphere depends on the characteristics of the cumulus parameterizations used. If the cumulus parameterization is able to amplify the SST-initiated surface disturbances through sustaining a robust upward–downward feedback as revealed in Figs. 10 and 11, the model will be able to capture the realistic SST feedback to the MJO (e.g., with the RAS); otherwise, the model will fail to produce any robust SST feedback (e.g., with the SAS2). Since the upward–downward feedback is also an essential process to sustain the atmospheric internal MJO mode (e.g., Kim and Seo 2018), the present findings further emphasize the notion that if an atmospheric model has a too weak internal MJO mode, most likely the effect of air–sea coupling on the MJO will be underestimated, too (Klingaman and Woolnough 2014; Fu et al. 2017).

5. Methods to quantify the relative contributions of atmospheric internal dynamics and SST feedback

Some previous studies have tried to quantify the impacts of air–sea coupling on intraseasonal variability
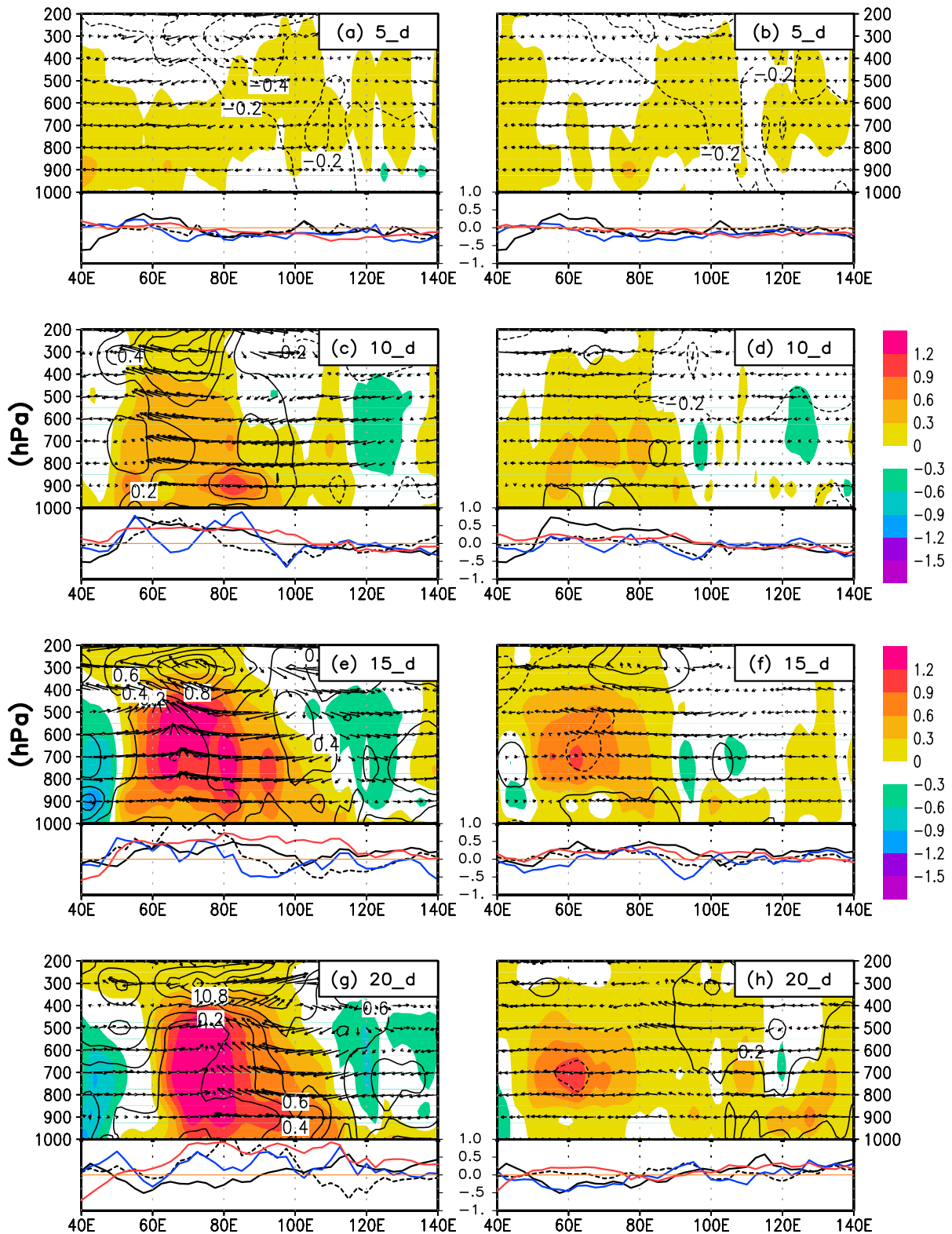
FIG. 10. Vertical cross sections (top part) of east–west anomalous circulations, air humidity (shading, $kg\ kg^{-1}$), and temperature anomalies (contours, CI: 0.2°C) along with (bottom part) SST (black solid line, °C/1.5), rainfall (black dashed line: $10\ mm\ day^{-2}$), surface evaporation (blue solid line: $40\ W\ m^{-2}$), and equivalent potential temperature (red solid line: 3 K) anomalies averaged between 10°S and 10°N for the RAS at days (a) 5, (c) 10, (e) 15, (g) 20 and the SAS2 at days (b) 5, (d) 10, (f) 15, (h) 20.
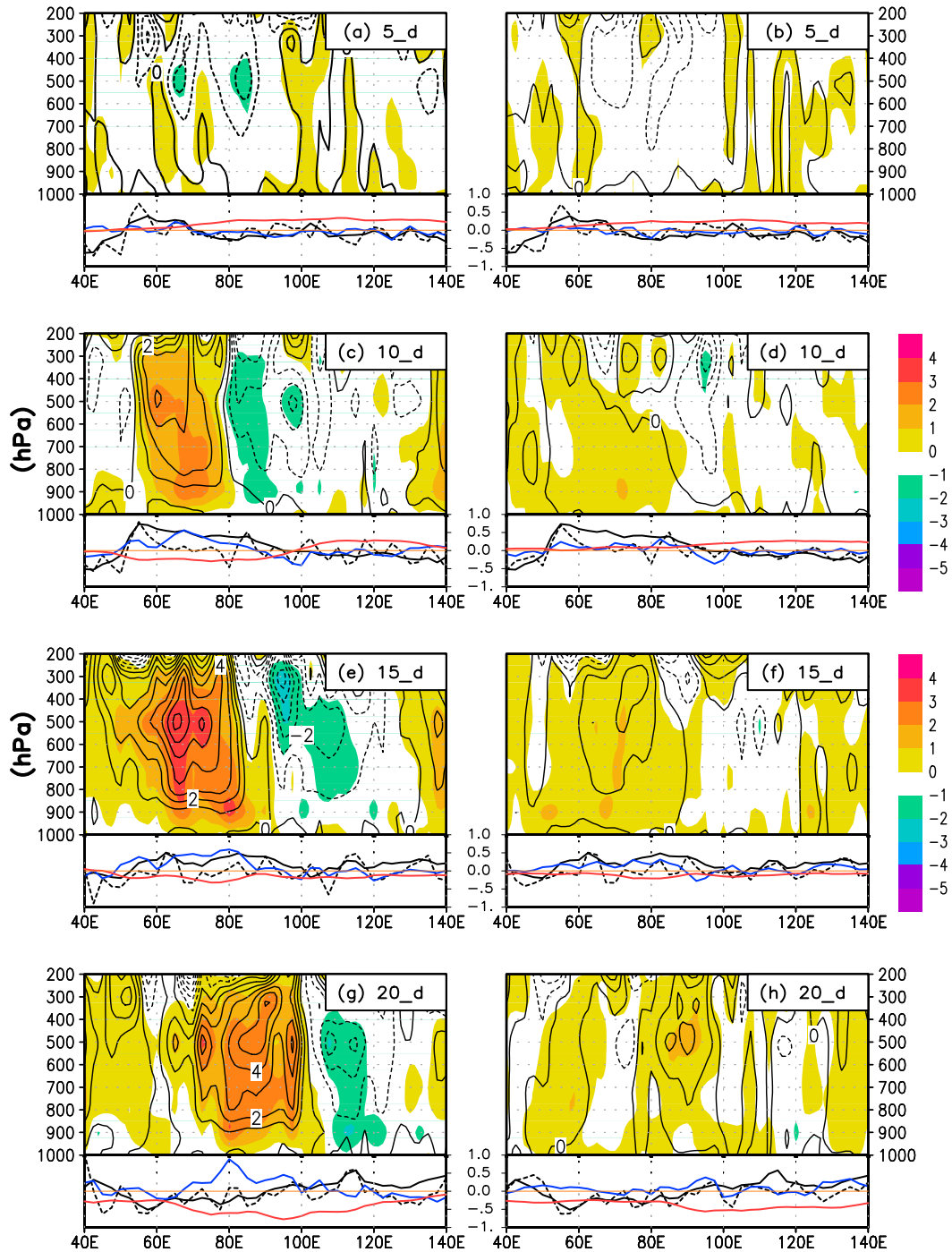
FIG. 11. As in Fig. 10, but for (top part) apparent moisture sink (shading, 1°C day^{-1}) and heat source (contours, CI: 1°C day^{-1}) along with (bottom part) SST (black solid line, °C/1.5), convergent Laplacian of SST (black dashed line: 3×10^{-12} °C m^{-2}), surface convergence (blue solid line: 4×10^{-6} s^{-1}), and sea level pressure (red solid line, $\times$ 200 Pa) anomalies.

based on wavenumber–frequency spectral intensity (Fu et al. 2003; Fu and Wang 2004), predictability (Fu et al. 2007, 2008, 2013), and local convergence contribution (Maloney and Kiehl 2002; Hendon 2005; Hsu and

Li 2012). The first two methods are based on the differences between model runs with and without air–sea coupling. The first method intends to quantify the differences between two long-term free runs. The second

method is very useful with short-term hindcast runs. The third method intends to estimate the effect of air–sea coupling directly from the observations (or reanalysis datasets). In recognizing that the third method only considered the local direct contribution from the SST gradient while the potential amplification from upward–downward feedback (Gill 1980; Wang and Li 1993; Chiang and Zebiak 2000; Fu et al. 2008; Back and Bretherton 2009a) and the cumulative effect during the MJO life cycle are not included, in this study, we attempt to revise this measure with the GFS hindcasts under the RAS scheme forced by the TMI and CLIM SSTs.

First, we introduce two new concepts that will be used to quantify the relative contributions of atmospheric internal dynamics and SST feedback: the "potential" ($ATM_{potential}$ and $SST_{potential}$) and "practical" ($ATM_{pratical}$ and $SST_{practical}$) contributions. To measure the potential contributions, we accumulate the total contributions from the atmospheric internal dynamics and SST feedback[6]:

$$ATM_{potential} = \frac{\sum P_{atm}}{\sum P_{TMI}}; \quad SST_{potential} = \frac{\sum (P_{TMI} - P_{atm})}{\sum P_{TMI}}. \quad (1)$$

The P_{atm} represents the contribution from atmospheric internal dynamics that can be calculated from the runs forced with the CLIM SST; the P_{TMI} represents the combined effect from atmospheric internal dynamics and SST feedback that can be assessed from the runs forced by TMI SST. Thus, $P_{TMI} - P_{atm}$ represents the contribution from SST feedback. The practical contributions from atmospheric internal dynamics ($ATM_{practical}$) and SST feedback ($SST_{practical}$) can be defined in a similar fashion as in Eq. (1), but the individual terms (i.e., P_{atm}, P_{TMI}, and $P_{TMI} - P_{atm}$) on the right-hand sides are constrained by observations.[7]

Since we have 61 daily forecasts (from 1 October to 30 November 2011) and each forecast has been integrated for 30 days, two different accumulation methods [the Σ in Eq. (1)] have been tested in this study: 1) accumulating over 61 forecasts at each lead time to obtain the contributions of atmospheric internal dynamics and SST feedback as a function of lead time (Figs. 12a,b) and 2) accumulating the first 25-day integration for each forecast to obtain the contributions of atmospheric internal dynamics and SST feedback as a function of initial times (Figs. 12c,d). The variables used to do the accumulations are precipitation and surface convergence.

With the first accumulation method (Figs. 12a,b), the potential contribution from the atmospheric internal dynamics in terms of precipitation and surface convergence is around 80% initially, but steadily drops to near zero at lead time of day 20 (Fig. 12a). The potential contribution from SST feedback, however, increases steadily from an initial 20% to about 100% at a lead time of day 20. For the practical contributions (Fig. 12b), the portion of atmospheric internal dynamics is again very high (more than 80%) initially, but steadily drops to zero around day 15, while the temporal evolution of the SST-feedback contribution shows just the opposite, steadily increasing from an initial 10% to 100% around day 15. In both the potential and practical cases, the contributions of SST feedback become larger than that of atmospheric internal dynamics after about one week.

With the second accumulation method (Figs. 12c,d), the averaged potential contribution from the atmospheric internal dynamics (SST feedback) is around 35% (65%), but at the same time it exhibits significant zigzag fluctuations with different initial dates (Fig. 12c). For example, the contribution of atmospheric internal dynamics varies from 20% to 40% when initialized on two consecutive days (e.g., 17 and 18 November). Whether this feature is model dependent warrants further study. It is very interesting to find out that the practical contributions of atmospheric internal dynamics and SST feedback vary dramatically from event to event as illustrated in Fig. 12d. During some periods (e.g., mid-October), the contribution from atmospheric internal dynamics is systematically larger than that from SST feedback, suggesting that the MJO during this period is primarily controlled by atmospheric internal dynamics. During the other periods (e.g., early November), the contribution from SST feedback is consistently higher than that from atmospheric internal dynamics. This result further corroborates our previous finding that the Oct-MJO is primarily governed by atmospheric internal dynamics while the Nov-MJO is strongly coupled to the underlying ocean (Fu et al. 2015, 2017). It is promising that these new methods proposed here are able to clearly separate the MJO events that are primarily governed by atmospheric internal dynamics from those strongly coupled to the underlying ocean. Future studies with hindcasts from multimodels covering many years are needed to further confirm how effectively these new methods can quantify the respective effects of air–sea coupling and atmospheric internal dynamics on the MJO.

---

[6] Since the intraseasonal SST anomaly results from air–sea interactions, the contribution of SST feedback in this study actually represents the effect of mutual atmosphere–ocean interactions.

[7] In this study, the "potential" and "practical" contributions are constrained by positive precipitation and surface convergence anomalies, respectively, from the run forced by TMI SST and observations (i.e., TRMM precipitation and CFSR surface convergence).
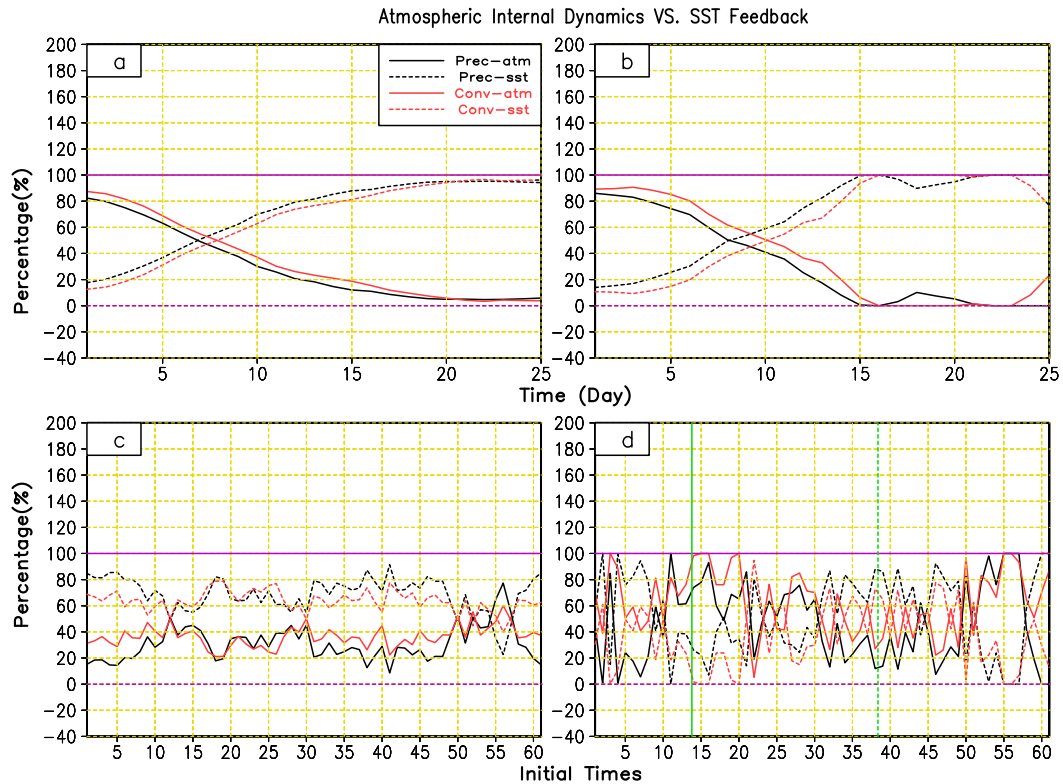
FIG. 12. Relative contributions of atmospheric internal dynamics and SST feedback on the MJOs [percentage (%)] during the DYNAMO period over the tropical Indian Ocean (15°S–15°N, 40°–100°E) as functions of (a),(b) lead time and (c),(d) initial times. The start time in (c) and (d) is 1 Oct 2011. The solid (dashed) lines in (a) and (c) represent the *potential* contributions from the atmospheric internal dynamics (SST feedback). The solid (dashed) lines in (b) and (d) represent the *practical* contributions from the atmospheric internal dynamics (SST feedback). The black and red lines represent the precipitation and surface convergence, respectively. The definition of potential and practical contributions is given in the text.

6. Conclusions and discussion

Our two recent studies (Wang et al. 2015; Fu et al. 2017) have shown that even forced with the same daily TMI SST, which has realistic intraseasonal variability (Harrison and Vecchi 2001; Chelton and Wentz 2005), the NCEP GFS under three different cumulus schemes (i.e., RAS, SAS, and SAS2) produces quite different MJO simulations. This paper investigates the diverse SST-feedback processes in association with each cumulus scheme. In addition, new methods were also developed to measure the respective contributions of atmospheric internal dynamics and SST feedback on the MJOs.

This study targeted two MJO events (i.e., the Oct- and Nov-MJO) that occurred during the DYNAMO field campaign. In total, six sets of hindcasts carried out in Wang et al. (2015) for this period have been used. The hindcasts were conducted, respectively, with three cumulus schemes under the TMI and climatological SST forcings. The differences between the runs forced by the TMI and climatological SSTs have been used to represent the effects of SST feedback. To unravel the SST-feedback processes, the relationships between the SST anomaly and atmospheric variables relevant to the responses to SST (e.g., surface convergence, latent heat flux, equivalent potential temperature, convection, apparent heat source and moisture sink, etc.) are comprehensively analyzed.

The SST anomaly and its convergent Laplacian (Li and Carbone 2012; Carbone and Li 2015) are always collocated (Figs. 4, 7, and 8). Both the positive SST anomaly and associated convergent Laplacian increase surface air temperature and humidity (Fig. 6), surface convergence (Lindzen and Nigam 1987), surface latent heat flux, and equivalent potential temperature (Figs. 2, 3, 4, 5, 7, and 8). These SST-initiated surface disturbances are very similar in the first several days' simulations no matter which cumulus scheme was used. These surface disturbances quickly excite convection, which is termed as "upward" impact. The elevated heating in association with the convection, on the other

hand, drives overturning circulations (Gill 1980), thus affecting surface disturbances, which is termed as "downward" impact. Although the downward impact has strong control on the spatiotemporal variations of surface latent heat flux (Figs. 3 and 4), it will not amplify the initial perturbations as much as for the surface convergence disturbances (Fig. 5). It is the strong upward–downward feedback between convection and surface convergence that leads to robust SST feedback. This feedback manifests much stronger in the RAS and SAS schemes than that in the S2S scheme (Figs. 2, 4, and 5).

The strong upward–downward feedback in the RAS scheme (Figs. 10 and 11) significantly amplifies the surface convergence initiated by the positive SST anomaly, which in turn moistens the troposphere and favors the development of deep convection and stratiform rainfall (Johnson et al. 2015). The resultant covariability between upper-tropospheric warming and heating facilitates the production of eddy available potential energy (Fu and Wang 2009; Fu et al. 2015), which is essential to sustain the large-scale circulations associated with enhanced MJO convection (Hendon and Salby 1994).

On the other hand, the upward–downward feedback in the SAS2 scheme is very weak (Figs. 10 and 11). The primary reasons may be threefold: (i) the upward moisture transport from the PBL to troposphere is too weak (Wang et al. 2015); (ii) the deep convection triggering is too loose; and (iii) the lack of stratiform rainfall. In fact, the SAS2 scheme is an updated version based on the RAS and SAS schemes. To suppress the grid-scale (stratiform) rainfall, Han and Pan (2011) relaxed the deep convection triggering and removed the random cloud-top scheme in the RAS scheme. To increase model stratocumulus, the shallow convection entrainment rate has been tuned down to a few times smaller than that derived from large-eddy simulation (Siebesma et al. 2003). As shown in our previous study (Fu and Wang 2009), the reduction of shallow convection entrainment and the suppression of model stratiform rainfall will lead to significant weakening of model MJO.

New methods to measure the relative contributions of atmospheric internal dynamics and SST feedback were also developed using the hindcasts with the RAS scheme forced by the TMI and climatological SSTs. Since the hindcast MJOs with the RAS scheme forced with the TMI SST is very similar to the observations (Wang et al. 2015; Fu et al. 2017), the difference between the runs forced by the TMI and climatological SSTs serves as a good indicator of the contribution of SST feedback. The run forced by the climatological SST has been used to represent the contribution from atmospheric internal dynamics. Based on Eq. (1), the "potential" and "practical"

contributions of the atmospheric internal dynamics and SST feedback have been assessed. The differences between the practical and potential contributions are that the former (latter) are constrained with the observations (the run forced by TMI SST).

Overall, the potential contributions from SST feedback are higher than that from atmospheric internal dynamics after about a 1-week lead time (Figs. 12a,c). When measuring the practical contributions as a function of lead time (Fig. 12b), the initial contribution from atmospheric internal dynamics (SST feedback) is over 80% (about 10%) but rapidly drops (increases) to close to zero (100%) around day 15. When measuring as a function of initial times (Fig. 12d), the practical contributions from atmospheric internal dynamics and SST feedback fluctuate considerably. During certain periods (e.g., mid-October: before and during the Oct-MJO active phase), atmospheric internal dynamics plays a dominant role. During other periods (e.g., early November: before and during the Nov-MJO active phase), the contribution from SST feedback is significantly stronger than that from atmospheric internal dynamics. Averaged over the entire period, the contributions from atmospheric internal dynamics and SST feedback are about half and half. These results are consistent with our previous findings (Fu et al. 2003, 2015, 2017).

The present results also suggest that the estimates from the observations in a few previous studies (e.g., Maloney and Kiehl 2002; Hendon 2005; Hsu and Li 2012) may considerably underestimate the contributions of air–sea coupling on the MJO intensity and life cycle. At the same time, we are also aware that the present results are derived from one model (NCEP GFS) with a short hindcast period (only during first two months of DYNAMO field campaign). It is still uncertain to what degree our findings are model dependent. Further studies with multimodels and longer periods are needed to confirm our present findings.

REFERENCES

Ajayamohan, R. S., H. Annamalai, J.-J. Luo, J. Hafner, and T. Yamagata, 2011: Poleward propagation of boreal summer intraseasonal oscillations in a coupled model: Role of internal processes. *Climate Dyn.*, **37**, 851–867, https://doi.org/10.1007/s00382-010-0839-6.

Arakawa, A., and W. H. Schubert, 1974: Interaction of a cumulus ensemble with the large-scale environment, part I. *J. Atmos. Sci.*, **31**, 674–704, https://doi.org/10.1175/1520-0469(1974)031<0674: IOACCE>2.0.CO;2.

Back, L. E., and C. S. Bretherton, 2009a: On the relationship between SST gradients, boundary layer winds, and convergence over the tropical oceans. *J. Climate*, **22**, 4182–4196, https://doi.org/10.1175/2009JCLI2392.1.

——, and ——, 2009b: A simple model of climatological rainfall and vertical motion patterns over the tropical oceans. *J. Climate*, **22**, 6477–6497, https://doi.org/10.1175/2009JCLI2393.1.

Bechtold, P., M. Köhler, T. Jung, F. Doblas-Reyes, M. Leutbecher, M. J. Rodwell, F. Vitart, and G. Balsamo, 2008: Advances in simulating atmospheric variability with the ECMWF model: From synoptic to decadal time-scale. *Quart. J. Roy. Meteor. Soc.*, **134**, 1337–1351, https://doi.org/10.1002/qj.289.

Carbone, R. E., and Y. Li, 2015: Tropical ocean rainfall and sea surface temperature structure: Parsing causation from correlation in the MJO. *J. Atmos. Sci.*, **72**, 2703–2717, https://doi.org/10.1175/JAS-D-14-0226.1.

Chelton, D. B., and F. J. Wentz, 2005: Global microwave satellite observations of sea surface temperature for numerical weather prediction and climate research. *Bull. Amer. Meteor. Soc.*, **86**, 1097–1115, https://doi.org/10.1175/BAMS-86-8-1097.

Chiang, J. C. H., and S. E. Zebiak, 2000: Surface wind over tropical oceans: Diagnosis of the momentum balance, and modeling the linear friction coefficient. *J. Climate*, **13**, 1733–1747, https://doi.org/10.1175/1520-0442(2000)013<1733:SWOTOD>2.0.CO;2.

de Boisséson, E., M. A. Balmaseda, F. Vitart, and K. Mogensen, 2012: Impact of the sea surface temperature forcing on hindcasts of Madden–Julian oscillation events using the ECMWF model. *Ocean Sci.*, **8**, 1071–1084, https://doi.org/10.5194/os-8-1071-2012.

DeMott, C. A., N. P. Klingaman, and S. J. Woolnough, 2015: Atmosphere-ocean coupled processes in the Madden–Julian oscillation. *Rev. Geophys.*, **53**, 1099–1154, https://doi.org/10.1002/2014RG000478.

de Szoeke, S. P., J. B. Edson, J. R. Marion, C. W. Fairall, and L. Bariteau, 2015: The MJO and air–sea interaction in TOGA COARE and DYNAMO. *J. Climate*, **28**, 597–622, https://doi.org/10.1175/JCLI-D-14-00477.1.

Eyring, V., S. Bony, G. A. Meehl, C. A. Senior, B. Stevens, R. J. Stouffer, and K. E. Taylor, 2016: Overview of the Coupled Model Intercomparison Project Phase 6 (CMIP6) experimental design and organization. *Geosci. Model Dev.*, **9**, 1937–1958, https://doi.org/10.5194/gmd-9-1937-2016.

Fu, R., A. D. Del Genio, and W. B. Rossow, 1994: Influence of ocean surface conditions on atmospheric vertical thermodynamic structure and deep convection. *J. Climate*, **7**, 1092–1108, https://doi.org/10.1175/1520-0442(1994)007<1092:IOOSCO>2.0.CO;2.

Fu, X., and B. Wang, 1999: On the role of longwave radiation and boundary layer thermodynamics on forcing tropical surface winds. *J. Climate*, **12**, 1049–1069, https://doi.org/10.1175/1520-0442(1999)012<1049:TROLRA>2.0.CO;2.

——, and ——, 2004: Differences of boreal summer intraseasonal oscillations simulated in an atmosphere–ocean coupled model and an atmosphere-only model. *J. Climate*, **17**, 1263–1271, https://doi.org/10.1175/1520-0442(2004)017<1263:DOBSIO>2.0.CO;2.

——, and ——, 2009: Critical roles of the stratiform rainfall in sustaining the Madden–Julian oscillation: GCM experiments. *J. Climate*, **22**, 3939–3959, https://doi.org/10.1175/2009JCLI2610.1.

——, ——, T. Li, and J. P. McCreary, 2003: Coupling between northward-propagating intraseasonal oscillations and sea surface temperature in the Indian Ocean. *J. Atmos. Sci.*, **60**, 1733–1753, https://doi.org/10.1175/1520-0469(2003)060<1733:CBNIOA>2.0.CO;2.

——, ——, and L. Tao, 2006: Satellite data reveal the 3-D moisture structure of tropical intraseasonal oscillation and its coupling with underlying ocean. *Geophys. Res. Lett.*, **33**, L03705, https://doi.org/10.1029/2005GL025074.

——, ——, D. E. Waliser, and L. Tao, 2007: Impact of atmosphere–ocean coupling on the predictability of monsoon intraseasonal oscillations. *J. Atmos. Sci.*, **64**, 157–174, https://doi.org/10.1175/JAS3830.1.

——, B. Yang, Q. Bao, and B. Wang, 2008: Sea surface temperature feedback extends the predictability of tropical intraseasonal oscillation. *Mon. Wea. Rev.*, **136**, 577–597, https://doi.org/10.1175/2007MWR2172.1.

——, J.-Y. Lee, P.-C. Hsu, H. Taniguichi, B. Wang, W. Wang, and S. Weaver, 2013: Multi-model MJO forecasting during DYNAMO/CINDY period. *Climate Dyn.*, **41**, 1067–1081, https://doi.org/10.1007/s00382-013-1859-9.

——, W. Wang, J.-Y. Lee, B. Wang, K. Kikuchi, J. Xu, J. Li, and S. Weaver, 2015: Distinctive roles of air–sea coupling on different MJO events: A new perspective revealed from the DYNAMO/CINDY field campaign. *Mon. Wea. Rev.*, **143**, 794–812, https://doi.org/10.1175/MWR-D-14-00221.1.

——, ——, T. Shinoda, H.-L. Ren, and X. Jia, 2017: Toward understanding the diverse impacts of air-sea interactions on MJO simulations. *J. Geophys. Res. Oceans*, **122**, 8855–8875, https://doi.org/10.1002/2017JC013187.

Gill, A. E., 1980: Some simple solutions for heat-induced tropical circulation. *Quart. J. Roy. Meteor. Soc.*, **106**, 447–462, https://doi.org/10.1002/qj.49710644905.

Grabowski, W. W., 2006: Impact of explicit atmosphere–ocean coupling on MJO-like coherent structures in idealized aquaplanet simulations. *J. Atmos. Sci.*, **63**, 2289–2306, https://doi.org/10.1175/JAS3740.1.

Han, J., and H.-L. Pan, 2011: Revision of convection and vertical diffusion schemes in the NCEP Global Forecast System. *Wea. Forecasting*, **26**, 520–533, https://doi.org/10.1175/WAF-D-10-05038.1.

Harrison, D. E., and G. A. Vecchi, 2001: January 1999 Indian Ocean cooling event. *Geophys. Res. Lett.*, **28**, 3717–3720, https://doi.org/10.1029/2001GL013506.

Hendon, H. H., 2000: Impact of air–sea coupling on the Madden–Julian oscillation in a general circulation model. *J. Atmos. Sci.*, **57**, 3939–3952, https://doi.org/10.1175/1520-0469(2001)058<3939:IOASCO>2.0.CO;2.

——, 2005: Air–sea interaction. *Intraseasonal Variability in the Atmosphere–Ocean Climate System*, W. K.-M. Lau and D. E. Waliser, Eds., Springer, 247–266.

——, and M. L. Salby, 1994: The life cycle of the Madden–Julian oscillation. *J. Atmos. Sci.*, **51**, 2225–2237, https://doi.org/10.1175/1520-0469(1994)051<2225:TLCOTM>2.0.CO;2.

Hirst, A. C., 1986: Unstable and damped equatorial modes in simple coupled ocean–atmosphere models. *J. Atmos. Sci.*, **43**, 606–630, https://doi.org/10.1175/1520-0469(1986)043<0606:UADEMI>2.0.CO;2.

Hsu, P.-C., and T. Li, 2012: Role of the boundary layer moisture asymmetry in causing the eastward propagation of the Madden–Julian oscillation. *J. Climate*, **25**, 4914–4931, https://doi.org/10.1175/JCLI-D-11-00310.1.

Inness, P. M., J. M. Slingo, E. Guilyardi, and J. Cole, 2003: Simulation of the Madden–Julian oscillation in a coupled general circulation model. Part II: The role of the basic state. *J. Climate*, **16**, 365–382, https://doi.org/10.1175/1520-0442(2003)016<0365:SOTMJO>2.0.CO;2.

Johnson, R. H., P. E. Ciesielski, J. H. Ruppert Jr., and M. Katsumata, 2015: Sounding-based thermodynamic budget for DYNAMO. *J. Atmos. Sci.*, **72**, 598–622, https://doi.org/10.1175/JAS-D-14-0202.1.

Kawamura, R., 1988: Intraseasonal variability of sea surface temperature over the tropical western Pacific. *J. Meteor. Soc. Japan*, **66**, 1007–1012, https://doi.org/10.2151/jmsj1965.66.6_1007.

Kim, G.-U., and K.-H. Seo, 2018: Identifying a key physical factor sensitive to the performance of Madden–Julian oscillation simulation in climate models. *Climate Dyn.*, **50**, 391–401, https://doi.org/10.1007/s00382-017-3616-y.

Klingaman, N. P., and S. J. Woolnough, 2014: The role of air–sea coupling in the simulation of the Madden–Julian oscillation in the Hadley Centre model. *Quart. J. Roy. Meteor. Soc.*, **140**, 2272–2286, https://doi.org/10.1002/qj.2295.

Krishnamurti, T. N., D. K. Oosterhof, and A. V. Mehta, 1988: Air–sea interaction on the timescale of 30 to 50 days. *J. Atmos. Sci.*, **45**, 1304–1322, https://doi.org/10.1175/1520-0469(1988)045<1304:AIOTTS>2.0.CO;2.

Lau, K.-H., and N.-C. Lau, 1992: The energetics and propagation dynamics of tropical summertime synoptic-scale disturbances. *Mon. Wea. Rev.*, **120**, 2523–2539, https://doi.org/10.1175/1520-0493(1992)120<2523:TEAPDO>2.0.CO;2.

Lau, K.-M., and C.-H. Sui, 1997: Mechanisms of short-term sea surface temperature regulation: Observations during TOGA COARE. *J. Climate*, **10**, 465–472, https://doi.org/10.1175/1520-0442(1997)010<0465:MOSTSS>2.0.CO;2.

Li, Y., and R. E. Carbone, 2012: Excitation of rainfall over the tropical western Pacific. *J. Atmos. Sci.*, **69**, 2983–2994, https://doi.org/10.1175/JAS-D-11-0245.1.

Lindzen, R. S., and S. Nigam, 1987: On the role of sea surface temperature gradients in forcing low-level winds and convergence in the tropics. *J. Atmos. Sci.*, **44**, 2418–2436, https://doi.org/10.1175/1520-0469(1987)044<2418:OTROSS>2.0.CO;2.

Madden, R. A., and P. R. Julian, 1971: Detection of a 40–50-day oscillation in zonal wind in the tropical Pacific. *J. Atmos. Sci.*, **28**, 702–708, https://doi.org/10.1175/1520-0469(1971)028<0702:DOADOI>2.0.CO;2.

——, and ——, 1972: Description of global-scale circulation cells in the tropics with a 40–50 day period. *J. Atmos. Sci.*, **29**, 1109–1123, https://doi.org/10.1175/1520-0469(1972)029<1109:DOGSCC>2.0.CO;2.

Maloney, E. D., and J. T. Kiehl, 2002: MJO-related SST variations over the tropical eastern Pacific during Northern Hemisphere summer. *J. Climate*, **15**, 675–688, https://doi.org/10.1175/1520-0442(2002)015<0675:MRSVOT>2.0.CO;2.

Marshall, A. G., O. Alves, and H. H. Hendon, 2008: An enhanced moisture convergence–evaporation feedback mechanism for MJO air–sea interaction. *J. Atmos. Sci.*, **65**, 970–986, https://doi.org/10.1175/2007JAS2313.1.

Miura, H., M. Satoh, T. Nasuno, A. T. Noda, and K. Oouchi, 2007: A Madden-Julian oscillation event realistically simulated by a global cloud-resolving model. *Science*, **318**, 1763–1765, https://doi.org/10.1126/science.1148443.

Moorthi, S., and M. J. Suarez, 1992: Relaxed Arakawa-Schubert: A parameterization of moist convection for general circulation model. *Mon. Wea. Rev.*, **120**, 978–1002, https://doi.org/10.1175/1520-0493(1992)120<0978:RASAPO>2.0.CO;2.

——, and ——, 1999: Documentation of version 2 of relaxed Arakawa-Schubert cumulus parameterization with convective downdrafts. NOAA Office Note 99-01, 44 pp.

National Research Council, 2010: *Assessment of Intraseasonal to Interannual Climate Prediction and Predictability*. National Academies Press, 192 pp.

Neelin, J. D., 1989: On the interpretation of the Gill model. *J. Atmos. Sci.*, **46**, 2466–2468, https://doi.org/10.1175/1520-0469(1989)046<2466:OTIOTG>2.0.CO;2.

——, and I. M. Held, 1987: Modeling tropical convergence based on the moist static energy budget. *Mon. Wea. Rev.*, **115**, 3–12, https://doi.org/10.1175/1520-0493(1987)115<0003:MTCBOT>2.0.CO;2.

Newman, M., P. D. Sardeshmukh, and C. Penland, 2009: How important is air–sea coupling in ENSO and MJO evolution? *J. Climate*, **22**, 2958–2977, https://doi.org/10.1175/2008JCLI2659.1.

Pan, H.-L., and W.-S. Wu, 1995: Implementing a mass flux convection parameterization package for the NMC medium-range forecast model. NMC Office Note 409, 39 pp.

Pegion, K., and B. P. Kirtman, 2008: The impact of air–sea interactions on the predictability of the tropical intraseasonal oscillation. *J. Climate*, **21**, 5870–5886, https://doi.org/10.1175/2008JCLI2209.1.

Philander, S. G. H., T. Yamagata, and R. C. Pacanowski, 1984: Unstable air–sea interactions in the tropics. *J. Atmos. Sci.*, **41**, 604–613, https://doi.org/10.1175/1520-0469(1984)041<0604:UASIIT>2.0.CO;2.

Riley Dellaripa, E. M., and E. D. Maloney, 2015: Analysis of MJO wind-flux feedbacks in the Indian Ocean using RAMA buoy observations. *J. Meteor. Soc. Japan*, **93A**, 1–20, https://doi.org/10.2151/jmsj.2015-021.

Roxy, M., and Y. Tanimoto, 2007: Role of SST over the Indian Ocean in influencing the intraseasonal variability of the Indian summer monsoon. *J. Meteor. Soc. Japan*, **85**, 349–358, https://doi.org/10.2151/jmsj.85.349.

Saha, S., and Coauthors, 2010: The NCEP Climate Forecast System Reanalysis. *Bull. Amer. Meteor. Soc.*, **91**, 1015–1057, https://doi.org/10.1175/2010BAMS3001.1.

——, and Coauthors, 2014: The NCEP Climate Forecast System version 2. *J. Climate*, **27**, 2185–2208, https://doi.org/10.1175/JCLI-D-12-00823.1.

Schneider, E. K., and R. S. Lindzen, 1977: Axially symmetric steady-state models of the basic state for instability and climate studies. Part I. Linearized calculations. *J. Atmos. Sci.*, **34**, 263–279, https://doi.org/10.1175/1520-0469(1977)034<0263:ASSSMO>2.0.CO;2.

Shinoda, T., H. H. Hendon, and J. Glick, 1998: Intraseasonal variability of surface fluxes and sea surface temperature in the tropical western Pacific and Indian Oceans. *J. Climate*, **11**, 1685–1702, https://doi.org/10.1175/1520-0442(1998)011<1685:IVOSFA>2.0.CO;2.

Siebesma, A. P., and Coauthors, 2003: A large eddy simulation intercomparison study of shallow cumulus convection. *J. Atmos. Sci.*, **60**, 1201–1219, https://doi.org/10.1175/1520-0469(2003)60<1201:ALESIS>2.0.CO;2.

Stephens, G. L., P. J. Webster, R. H. Johnson, R. Engelen, and T. L'Ecuyer, 2004: Observational evidence for the mutual regulation of the tropical hydrological cycle and tropical sea surface temperatures. *J. Climate*, **17**, 2213–2224, https://doi.org/10.1175/1520-0442(2004)017<2213:OEFTMR>2.0.CO;2.

Waliser, D. E., K. M. Lau, and J.-H. Kim, 1999: The influence of coupled sea surface temperatures on the Madden–Julian

oscillation: A model perturbation experiment. *J. Atmos. Sci.*, **56**, 333–358, https://doi.org/10.1175/1520-0469(1999)056<0333:TIOCSS>2.0.CO;2.

Wang, B., and T. Li, 1993: A simple tropical atmospheric model of relevance to short-term climate variations. *J. Atmos. Sci.*, **50**, 260–284, https://doi.org/10.1175/1520-0469(1993)050<0260:ASTAMO>2.0.CO;2.

Wang, L., T. Li, E. Maloney, and B. Wang, 2017: Fundamental causes of propagating and non-propagating MJOs in MJOTF/GASS models. *J. Climate*, **30**, 3743–3769, https://doi.org/10.1175/JCLI-D-16-0765.1.

Wang, W., A. Kumar, J. X. Fu, and M.-P. Hang, 2015: What is the role of the sea surface temperature uncertainty in the prediction of tropical convection associated with MJO? *Mon. Wea. Rev.*, **143**, 3156–3174, https://doi.org/10.1175/MWR-D-14-00385.1.

Wentz, F. J., C. Gentemann, D. Smith, and D. Chelton, 2000: Satellite measurements of sea surface temperature through clouds. *Science*, **288**, 847–850, https://doi.org/10.1126/science.288.5467.847.

Wu, Z., 2003: A shallow CISK, deep equilibrium mechanism for the interaction between large-scale convection and large-scale circulations in the tropics. *J. Atmos. Sci.*, **60**, 377–392, https://doi.org/10.1175/1520-0469(2003)060<0377:ASCDEM>2.0.CO;2.

Zebiak, S. E., 1986: Atmospheric convergence feedback in a simple model for El Niño. *Mon. Wea. Rev.*, **114**, 1263–1271, https://doi.org/10.1175/1520-0493(1986)114<1263:ACFIAS>2.0.CO;2.

——, and M. A. Cane, 1987: A model El Niño–Southern Oscillation. *Mon. Wea. Rev.*, **115**, 2262–2275, https://doi.org/10.1175/1520-0493(1987)115<2262:AMENO>2.0.CO;2.